CWV-Net: a Deep Neural Network for Atmospheric Column Water Vapor retrieval from Hyperspectral VNIR data

N. Acito[(1),(2)], M. Diani[(1),(2)], G. Corsini[(3)]
[(1)] Accademia Navale – Dip. Armi Navali – Viale Italia 72 – 57127 Livorno (Italy)
[(2)] Consorzio Nazionale Interuniversitario per le Telecomunicazioni – CNIT - Viale G.P. Usberti, 181/A -43124 Parma (Italy)
[(3)] Dipartimento di Ingegneria dell'Informazione-Università di Pisa-via G. Caruso 16 – 56122 Pisa (Italy)

e-mail: n.acito@iet.unipi.it, m.diani@iet.unipi.it, g.corsini@iet.unipi.it

***Abstract*—Estimation of the total Column Water Vapor (CWV) content of the atmosphere plays an important role in the atmospheric compensation of remotely sensed hyperspectral images collected in the Visible and Near InfraRed (VNIR) spectral range. Most of the proposed CWV retrieval methods provide accurate estimates as long as other significant atmospheric parameters are known. Those parameters are not generally available and must in turn be estimated. In this work, a new approach based on Deep Learning is proposed that allows the estimation of CWV without the knowledge of the atmospheric visibility, the solar zenith angle and the atmospheric point spread function. The proposed approach includes a training strategy based on synthetic data that are generated according to an accurate radiative transfer model and by exploiting reflectance spectral libraries and the Modtran radiative transfer code.**

Experiments on simulated data are carried out to analyze the performance of the proposed Deep Neural Network with reference to both aerial and satellite applications. Furthermore, an example of the results provided by the network in a real application is shown. For this purpose, the network is applied to data acquired by an airborne hyperspectral sensor operating in the VNIR spectral range.

***Index Terms*— Atmospheric compensation, water vapor retrieval, Hyperspectral Imagery.**

I. Introduction

Hyperspectral sensors (HSs) collecting data in the Visible and Near Infrared spectral range (VNIR) have gained the interest of the scientific community in the last years, especially thanks to the recent development of new generation sensors operating on board of UAV and drones ([1], [2], [3]). The major advantage offered by hyperspectral technology with respect to other remote sensing systems is the possibility of exploiting the physical and chemical composition of the observed surface through its spectral reflectance. Unfortunately, due to the distortion introduced by the atmosphere in the radiative transfer path, HSs do not measure directly the spectral reflectance of the monitored surface but rather the at-sensor radiance. Thus, acquired data must be processed in order to remove from the measured at-sensor radiance the contributions due to the solar illumination and the atmospheric effects. Such a process is generally referred to as Atmospheric Compensation (AC [4], [5]) and plays a crucial role in the exploitation of hyperspectral data. AC is a very challenging task as the effect of solar illumination and the distortion induced by the atmosphere depends on several factors, mainly aerosol scattering and water vapor absorption, many of which are not measurable at the acquisition time in most of practical applications.

Among the numerous AC techniques proposed in the past the most accurate and reliable are the physics-based ones that exploit analytical models of the radiative transfer (Radiative Transfer Models – RTMs, [6], [7], [8], [9]) in order to accounts for the absorption and scattering from atmospheric components and the acquisition geometry. Physics-based (or RTM based) AC methods generally deal with two distinct issues ([10]): 1) estimation of the atmospheric parameters of the RTM and 2) inversion of the model for spectral reflectance retrieval.

Usually, the parameters of the RTM related to the acquisition geometry are obtained from the mission planning or can be derived from the on board instrumentation. The remaining parameters can be only estimated by the observed data. For the VNIR spectral range the relevant RTM parameters are the meteorological range or atmospheric visibility (V) and the total column water vapor concentration (CWV) of the atmosphere. V can be reasonably considered constant all over the scene and is generally estimated by analyzing specific regions of the acquired image using methods such as the Dense Dark Vegetation (DDV [11]), the Boundary Shaded Pixels algorithm ([9]) or by exploiting a reference (Lambertian) target deployed in the monitored scene with known spectral reflectance.

The column water vapor concentration is generally spatially variant and its estimation needs a pixel level approach.

Several *CWV* retrieval algorithms resort to the differential absorption approach. For instance, such an approach is used by the AC commercial software package named Fast Line-of-Sight Atmospheric Analysis of Spectral Hypercubes (FLAASH, [12]). One of the most popular *CWV* retrieval algorithm is the Atmospheric Precorrected Differential Absorption Technique (APDA) proposed in [13] and included in the Airborne

Atmospheric and Topographic Correction (ATCOR, [14]) software package.

APDA makes use of the at-sensor radiance values in three groups of channels: the measurement channels with spectral central wavelength falling within a given atmospheric water vapor absorption region (typically around 820 nm or 940 nm) and two "reference" channels corresponding to the wavelengths located at each side of the water absorption band where absorption due to *CWV* is actually negligible. Those at-sensor radiance data are combined to compute the "depth" of the absorption feature that is related to *CWV*. The computed "depth" is compared with a pre-calculated look up table (LUT) to obtain the estimate of the *CWV* parameter.

APDA makes use of two simplifying assumptions: 1) the effects of the radiation of the surfaces surrounding the considered pixel (adjacency effect) are neglected; 2) the value of the spectral reflectance in the measurement channel is set to a fixed value (0.4) regardless of the observed surface. Both the hypotheses are not realistic. It is well-known that adjacency effects are not negligible in real hyperspectral data ([14], [15]). Furthermore, the spectral reflectance in the measurement channel strongly depends on the observed surface. Recently ([17]), by analyzing the performance of APDA using a more realistic and well-established RTM ([10]), it has been shown that the impact of such hypotheses is not negligible. To overcome the drawbacks of the APDA, in [17], the Low Rank Subspace projection based Water Estimator (LRSWE) was proposed. LRSWE is a *CWV* retrieval algorithm that exploits a more realistic RTM accounting for the adjacency effects and addresses the variability of the spectral reflectance of the observed surface in the water absorption bands by resorting to a low rank subspace representation. In LRSWE *CWV* estimates are obtained by solving a nonlinear least square optimization problem making use of specific LUT derived by the MODTRAN ([18]) radiative transfer code.

LRSWE outperforms APDA in *CWV* retrieval even in the presence of noise. However, the practical application of the algorithm has some critical aspects. Firstly, the LUT adopted by the algorithm (as well as that used by APDA) are derived assuming known some RTM parameters such as the flight height h, the solar zenith angle ϑ and the atmospheric visibility *V*. Generally, h is obtained with high accuracy from the flight operation planning; ϑ can be derived from the acquisition date and time, while *V* is estimated by image-based algorithms (such as those cited above) and represents the main source of uncertainty in atmospheric compensation. Of course, errors in the values assigned to the three parameters negatively affect *CWV* estimation performance. Secondly, to account for the adjacency effects LRSWE makes use of the adjacent at-sensor radiance that is obtained as a linear combination of the radiances of a neighborhood of the pixel under consideration. The weights adopted in the linear combination should be set according to the atmospheric Point Spread Function ([19]) that is not generally known. Since PSF estimation is a very challenging task, it is a common practice in hyperspectral atmospheric compensation ([14], [20]) to refer to standard PSF models by introducing an uncertainty in the derivation of the adjacent at-sensor radiance.

This has motivated us to develop a new strategy to provide accurate estimates for *CWV* regardless of the perfect knowledge of all the parameters of the RTM (specifically *V* and ϑ) and the atmospheric PSF. To obtain such a general algorithm we exploit the potential of the deep learning (DL).

DL allows models with increasingly higher semantic layers and complexity to be derived from the data themselves through a learning process. This makes DL a promising approach to achieve high precision and flexibility in solving very complex problems. DL has shown to yield remarkable results in a large number of applications concerning image analysis and speech processing. In the last few years, DL has been successfully applied to hyperspectral images to perform various tasks ([21], [22]) mainly concerning classification, feature extraction and noise mitigation. DL classification algorithms exploiting the spectral features of hyperspectral pixels were proposed in [23] and [24], while DL approaches based on the exploitation of the spatial features can be found in [25] and [26]. Recently, DL algorithms able to analyze both spectral and spatial features have been proven to enhance the classification accuracy ([27]). DL techniques, e.g. stacked autoencoders and convolutional neural networks (CNNs), are also used for spectral-spatial feature extraction ([28], [29]) and image denoising ([30], [31]). To the best of our knowledge, no work has been yet published concerning the application of DL techniques to the estimation of RTM parameters.

In this paper, we investigate the application of Deep Neural Networks (DNNs) to *CWV* retrieval. Specifically, we analyze a 1D-CNN based architecture named CWV-Net for estimating the total column water vapor concentration of the atmosphere in the VNIR spectral range from each pixel of a given hyperspectral image. CWV-Net is designed and trained to provide *CWV* estimates, without specific knowledge about the solar zenith angle and the atmospheric visibility. The only parameter to be set is the flight height h. Training is performed over hyperspectral data synthetized by means of a simulation strategy powered by the MODTRAN radiative transfer code and exploiting the availability of spectral reflectance libraries.

The paper is organized as follows. In Section II, we briefly summarize the RTM while in Section III we introduce the network architecture. In Section IV, we describe the strategy adopted to train the network by detailing the methodology for simulating the training data. Section V is dedicated to an extensive analysis of the performance provided by the proposed DL based algorithm on simulated data together with the comparison between CWV-Net and the LRSWE algorithm. We conclude the paper with a proof of concept concerning the application of CWV-Net to a real hyperspectral image.

II. Radiative Transfer Model for VNIR hyperspectral images

In this Section we introduce the RTM that is generally adopted ([8], [9]) to characterize the radiative transfer in the atmosphere in the VNIR spectral range. The RTM is a fundamental part of the proposed DL based estimation strategy as it is used in the construction of the training set adopted in the network learning.

Let us start by denoting as $L(\lambda)$ the at-sensor spectral radiance from the observed ground resolution cell in the sensor channel with central wavelength λ. It can be expressed as:

$$L(\lambda) = L_{GND}(\lambda, \mathbf{\Gamma}, CWV) + L_p(\lambda, \mathbf{\Gamma}, CWV) \quad (1)$$

where $L_p(\lambda, \mathbf{\Gamma}, CWV)$ is the intrinsic upwelling atmospheric spectral radiance and $L_{GND}(\lambda, \mathbf{\Gamma}, CWV)$ is the spectral radiance reaching the sensor after the interaction with the ground surface (ground reflected radiance). Both depend on the parameters specifying the acquisition geometry, the effects of absorption by gases in the atmosphere and scattering by molecules and aerosol. In general, the acquisition geometry parameters include the sun zenith (ϑ) and azimuth angles, the sensor zenith and azimuth angles, the sensor altitude (h) and the terrain elevation. In this work we assume that data are acquired from nadir view and that the monitored scene is flat. Thus, the relevant parameters for acquisition geometry characterization are ϑ and h.

The scattering effects are defined by the aerosol type and the atmospheric visibility (V). The aerosol type depends on the geographical position of the monitored scene, on the seasonal characteristics at the acquisition time, and, in general, on the concentration of the various contents of the atmosphere. The absorption effects depend on the concentration of the gases in the atmosphere. In the VNIR spectral range absorption is determined by the oxygen, which affects very narrow portions of the electromagnetic spectrum, by the ozone, whose effects are well modelled by standard concentration values, and mainly by the water vapor which is characterized by the total column water vapor concentration CWV. In eq. (1), we decoupled the parameter CWV by the rest of the atmospheric model parameters that are grouped in the vector $\mathbf{\Gamma}$.

The ground reflected radiance $L_{GND}(\lambda, \mathbf{\Gamma}, CWV)$ is generally modelled as ([8], [9], [14], [15]):

$$L_{GND}(\lambda, \mathbf{\Gamma}, CWV) = \frac{E_g(\lambda)}{\pi}\left[\tau_1(\lambda, \mathbf{\Gamma}, CWV)\frac{\rho(\lambda)}{1 - S(\lambda, \mathbf{\Gamma}, CWV)\rho_a(\lambda)} + \tau_2(\lambda, \mathbf{\Gamma}, CWV)\frac{\rho_a(\lambda)}{1 - S(\lambda, \mathbf{\Gamma}, CWV)\rho_a(\lambda)}\right] \quad (2)$$

In eq. (2), $E_g(\lambda)$ is the solar spectral irradiance incident on the ground, $\rho(\lambda)$ and $\rho_a(\lambda)$ are the spectral reflectances of the observed surface and of the adjacent surfaces, respectively. The term $\tau_1(\lambda, \mathbf{\Gamma}, CWV)$ accounts for the interaction of the surface material with the direct and diffuse solar radiation, while $\tau_2(\lambda, \mathbf{\Gamma}, CWV)$ accounts for the part of the solar radiation that, after the interaction with the materials in a neighborhood of the surface of interest, is scattered by the atmosphere in the sensor Instantaneous Field Of View (IFOV). Finally, the contributions due to multiple scattering are addressed by the term $1 - S(\lambda, \mathbf{\Gamma}, CWV)\rho_a(\lambda)$ with $S(\lambda, \mathbf{\Gamma}, CWV)$ denoting the spectral spherical albedo of the atmosphere.

The RTM in eqs. (1) and (2) refer to a Lambertian observed surface. Thus, $\rho(\lambda)$ is the isotropic spectral reflectance usually named hemispherical-directional reflectance factor (HDRF, [32]). Generally, $\rho(\lambda)$ can be viewed as a scaled version of the "absolute" surface reflectance ([4]) in that it does not address the anisotropic reflective behavior of the surface. Furthermore, it is worth noting that the presented model refers to clear sky condition that is the desirable condition for hyperspectral data collection.

III. CWV-NET ARCHITECTURE.

The goal of CWV-Net is the estimation of the atmospheric parameter CWV in each pixel of the hyperspectral image when one has no knowledge of the atmospheric visibility (V), of the solar zenith angle (ϑ) and of the atmospheric PSF. Only the sensor altitude h and the generic knowledge of the parameters related to aerosol scattering (that will be detailed in the next section) are required. To accomplish the above cited estimation task we resort to the potential of DNNs.

DNNs have several hidden layers and have been shown to be able to represent complicated data structures. A DNN takes advantages from its multi-levels architecture to obtain hierarchical feature representation of the data of interest. The parameters of each layer of a DNN are generally initialized randomly and finely tuned in a supervised manner by using labelled data and an error back-propagation algorithm. The number of the parameters to be learned in a DNN is very high and grows with the number of hidden layers. This is one of the factors that has limited the use of DNNs in the past. The huge number of DNN's parameters along with the limited number of available training data cause overfitting and a low capability of generalization. These issues are partially solved by the introduction of the CNN architecture ([33]) that exploits the ideas of local connections and shared weights within the hidden layers to obtain deep networks with a number of parameters smaller than those characterizing the DNNs based on dense layers.

Since we are interested into estimating CWV from the at-sensor spectral radiance measured by a hyperspectral sensor, in this work we focus on the class of 1D-CNN (one Dimensional-CNN) based DNN for regression. Such class of DNN have a general common architecture comprising:

1) one input layer;
2) one or more 1D-CNN hidden layers that are in charge of extracting hierarchically the significant features from the data;
3) one or more fully connected layers (Multi Layer Perceptrons - MLP) that, by exploiting the extracted features, estimate the parameter of interest.

The generic *l*-th 1D-CNN layer works on the features extracted by the previous layer and provides a new set of features. It has a fixed number K_l of kernels (or filters) having size $T_l \times 1$, that slide (convolve) along the layer input data dimension. The outputs of each kernel are modified by the activation function (which is generally non-linear). Finally, down sampling is performed on the output data by the pooling layer. It combines $P_l \times 1$ patches of its input data vector providing a single feature for each patch. Generally, such a feature is obtained by taking

the maximum (max-pooling) or averaging (average-pooling) over the patch values. The patches are selected sequentially over the data vector with a step of S_l (stride). Notice that, pooling can offer robustness to local features shift.

The proposed CWV-Net complies with the general architecture summarized above. The input vector for CWV-Net is the spectral radiance measured by the adopted hyperspectral sensor. Thus, the number of sensor channels defines the nodes of the input layer.

In this work, we refer to the SIM.GA ("Sistema Iperspettrale Modulare. Galileo Avionica") sensor, an avionic hyperspectral instrument manufactured by Leonardo-Finmeccanica covering the spectral range from 400 to 1000 nm with a spectral sampling of 1.2 nm. Generally, data acquired by the sensor are pre-processed by binning adjacent channels with a factor of two in order to reduce the effect of random noise. The resulting number of spectral channels is equal to 256. It is worth noting that, CWV estimation over vegetated pixels is generally biased by the leaf water content. It was shown that, water absorption features dominate the spectral reflectance of vegetation in the near-infrared region of the spectrum ([34]). Specifically, the first significant absorption can be approximately located from 925 nm to 1000 nm ([34], [35]). Thus, to avoid leaf water content bias over vegetated areas, we limit the spectral radiance provided by the sensor to 925 nm. The resulting number of spectral bands and, therefore, the number of nodes of the input layer of CWV-Net is 228.

The convolutional part of the proposed DNN has four 1D-CNN layers. In all of them, the activation function is the Rectified Linear Unit (ReLU) and down-sampling is obtained through max-pooling. The number and the size of the kernels along with the max-pooling dimension and stride in each 1D-CNN layer are summarized in Table I. The output of the convolutional part is a 64×1 feature vector.

Table I. Parameters of the convolutional layers: number of kernels K_l, size of each kernel T_l, max-pooling dimension P_l and stride S_l.

1D-CNN layer	K_l	T_l	P_l	S_l
1	4	4	4	4
2	16	4	4	4
3	32	4	4	4
4	64	1	3	3

The rest of CWV-Net comprises two fully-connected hidden layers having 32 and 16 nodes, respectively. The output layer has one single node being CWV-Net conceived for the estimation of a scalar parameter. The fully connected layers and the output layer have a ReLU activation function.

The complete architecture of CWV-Net is summarized in Figure 1. It is worth noting that, the input of the DNN is pre-processed to have unit Euclidean norm ("Data Normalization").

IV. CWV-Net Training

The learning phase of CWV-Net is performed by minimizing a given loss function through an error back-propagation algorithm over a training set.

The training set is obtained by simulation exploiting MODTRAN and a spectral reflectance library (**D**) obtained merging three different spectral libraries: ASTER ([36]), USGS (version released in 2007, [37]) and ANGERS ([38]) that contain the measured spectral reflectances of several man-made materials, vegetation, water, soils and minerals.

In this Section we describe the simulation strategy adopted to construct the training set and we introduce the loss function minimized in the learning stage.

A. Training set simulation strategy.

The t-th element of the training set is a pair comprising a value CWV_t of the column water vapor concentration and the corresponding at-sensor spectral radiance vector $\boldsymbol{L}_t(CWV_t)$. The element of the vectors are the values of the spectral radiance corresponding to the central wavelength of each band of the considered hyperspectral sensor.

$\boldsymbol{L}_t(CWV_t)$ is generated according to the RTM in eqs. (1) and (2) by means of the simulation strategy summarized in Figure 2.

Such a strategy comprises three main blocks. The first is the Reflectance Generator Block that simulates the surface spectral reflectance vector $\boldsymbol{\rho}_t$ and the adjacent spectral reflectance vector $\boldsymbol{\rho}_{a,t}$ from the elements of the library **D**. In order to increase the number and the variability of the spectral reflectance samples we use a data augmentation strategy based on the linear mixing model ([39]). Specifically:

$$\boldsymbol{\rho}_t = \sum_{i=1}^{5} a_i \mathbf{d}_i \qquad (3)$$

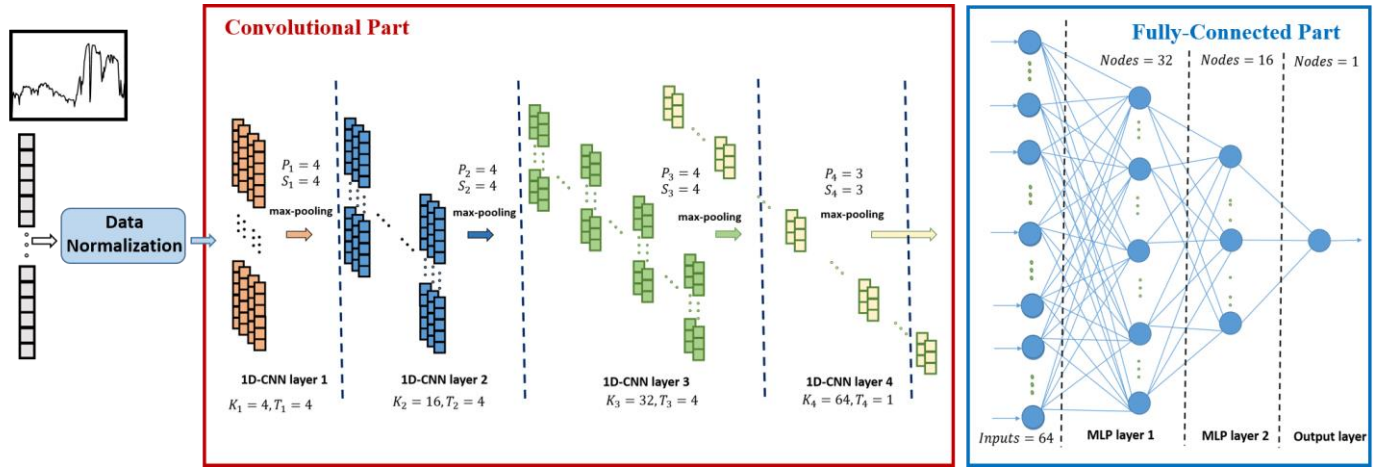

Figure 1. CWV-Net Architecture.

where $\mathbf{d}_i$ with $i = 1, \ldots, 5$ are the elements of **D** that acts as endmembers, and a_i with $i = 1, \ldots, 5$ are the abundances. The endmembers are selected randomly from **D** and the abundances are drawn from a Dirichlet distribution so as to meet the sum-to-one and the non-negative constraints. The same model is adopted to simulate $\boldsymbol{\rho}_{a,t}$, using new randomly selected endmembers and new randomly generated abundances. It is worth noting that, the use of the linear mixing model is a data augmentation strategy introduced to avoid overfitting over the spectra of the dictionary D and it is neither a requirement nor a fundamental hypothesis for the correct functioning of the proposed CWV retrieval algorithm.

The Atmosphere Generator Block is based on MODTRAN and generates the spectral vector of the radiometric quantities $\boldsymbol{E}_{g,t}$, $\boldsymbol{\tau}_{1,t}$, $\boldsymbol{\tau}_{2,t}$, $\boldsymbol{L}_{p,t}$ and $\boldsymbol{S}_t$ that appears in the RTM of eqs. (1) and (2). They are generated for a given set of the atmospheric model parameters required by MODTRAN: M, $IHAZE_t$, h, V_t, ϑ_t and, of course, CWV_t. The parameters M (called MODEL in MODTRAN) and $IHAZE_t$ specify the geographical and seasonal model and the aerosol model ([40]), respectively. The parameters h, V_t and ϑ_t (already introduced in Section I and II) represent the sensor height, the atmospheric visibility and the solar zenith angle.

The radiometric quantities and the reflectances $\boldsymbol{\rho}_t$ and $\boldsymbol{\rho}_{a,t}$, are combined according to the RTM defined by eqs. (1) and (2) to obtain the at-sensor spectral radiance vector $\mathbf{L}_t^*$ that is transformed in the sensor domain ($\mathbf{L}_t$) by the Sensor Block. It accounts for the Spectral Response Functions (SRFs) of the N_B sensor channels. Usually, a Gaussian shaped SRF is considered for each channel, It is characterized by the Full Width Half Maximum (FWHM) and the channel central wavelength (λ_n). In the case of the SIM.GA sensor the FWHM is 2.284 nm for each channel.

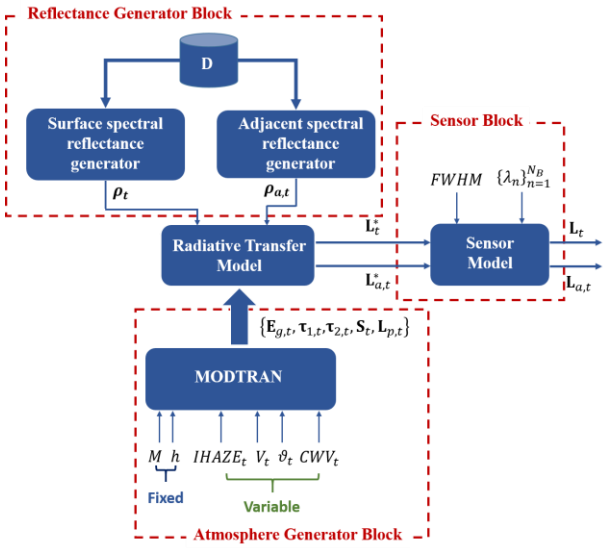

Figure 2. Block diagram of the simulation strategy

To construct the training set M and h are kept constant while the other parameters are made to vary. The values adopted for the variable parameters are shown in Table II.

For a value $\overline{CWV}$ of the total column water vapor concentration in Table II, 1000 different at-sensor spectral vectors $\mathbf{L}_t$ are generated according to the proposed simulation strategy and selecting randomly the other variable atmospheric parameters from the values in Table II. Thus, we obtain 1000 pairs $\{\mathbf{L}_t(\overline{CWV}), CWV_t = \overline{CWV}\}$. The procedure is repeated for each of the 46 values of the total column water vapor concentration in Table II, thus obtaining a total number of training pairs equal to 46000. Of course, before providing the predictors $\mathbf{L}_t(CWV_t)$ in input to CWV-Net, they are binned by a factor of two and the channels corresponding to wavelengths higher than 925 nm are discarded according to the input format defined in Section III.

B. Loss function for CWV-Net training.

The power of DNN depends on the connections (weights) of the entire network. These weights are "learned" during the training of the network by minimizing a chosen loss function over the training set pairs. In formulas:

$$\boldsymbol{\Omega} = \underset{\widetilde{\boldsymbol{\Omega}}}{arg\ min} \quad \underset{t=1,\dots,N}{loss}\left[g_{net}\left(\mathbf{L}_t, \widetilde{\boldsymbol{\Omega}}\right), CWV_t\right] \tag{4}$$

where, $\boldsymbol{\Omega}$ denotes the vector of the network weights, $g_{net}(\cdot)$ is the transformation operated by the network on the predictors (inputs), N is the total number of training pairs and $loss[\cdot]$ is the loss function computed over the entire training set. The loss function adopted to train CWV-Net is based on the Mean Absolute Percentage Error (MAPE) defined as:

$$MAPE\left(\widetilde{\boldsymbol{\Omega}}\right) = \frac{1}{N}\sum_{t=1}^{N}\frac{\left|g_{net}\left(\mathbf{L}_t, \widetilde{\boldsymbol{\Omega}}\right) - CWV_t\right|}{CWV_t} \cdot 100 \tag{5}$$

Typically, CWV has values ranging from 0.5 $g \cdot cm^{-2}$ (very dry atmosphere) to 5 $g \cdot cm^{-2}$ (very wet atmosphere). MAPE is chosen in order not to penalize small values of CWV.

Notice that CWV has positive values (>0.5) and this ensures the absence of division by zero and the non negativity of MAPE.

To limit the risk of overfitting, it is good practice to add a L2 regularization to the loss function ([41]). Thus:

$$loss\left(\widetilde{\boldsymbol{\Omega}}\right) = MAPE\left(\widetilde{\boldsymbol{\Omega}}\right) + \frac{\alpha}{2}\left\|\widetilde{\boldsymbol{\Omega}}\right\|^2 \tag{6}$$

where $\|\cdot\|^2$ denotes the L2-norm (Euclidean norm) and α is a free parameter that is tuned empirically (in our case we set $\alpha = 10^{-4}$).

The loss function in eq. (6) is minimized starting from randomly values for the network weights and using the Adam stochastic gradient-based optimizer ([42]).

Table II. Values adopted for the variable atmospheric parameters in the construction of the training set

Variable Atmospheric Parameters	
$IHAZE_t$	1 (Rural); 3 (Navy Maritime); 4 (Maritime); 5 (Urban); 10 (Desert)
$\vartheta_t(deg)$	0:10:70
$V_t(Km)$	10:10:60, 90, 120
$CWV_t\ (^{g}/_{cm^2})$	0.5:0.1:5

V. Results on simulated data

In this section, we analyze the performance of the CWV-Net on simulated data. The analysis aims to evaluate the ability of the network of estimating the values of CWV without any knowledge about the atmospheric visibility, the solar zenith angle and the adjacency effects. The analysis also aims to compare CWV-Net with the LRSWE algorithm and the APDA algorithm and to show the better flexibility that the DNN approach offers in typical operating conditions.

A. Experiments description and algorithms settings.

The analysis is carried out with reference to two scenarios. The first scenario concerns the aerial application. Specifically, we consider the case in which the airborne platform flies at 1 Km. The second scenario is related to a typical satellite application, where we have assumed a flight height of 600 Km[1]. In both the scenarios, we have assumed that the monitored scene is in the Mid-Latitude region and that data are collected during the summer.

To perform the analysis, two CWV-Net are trained by properly setting the fixed parameters M and h. Specifically, M is set to 2 that corresponds to the MODTRAN mid latitude summer model, while h is set to 1 Km and 600 Km, respectively in accordance with the two case studies. For the two networks, training is performed over more than 5000 epochs with a decreasing learning rate (it starts from 0.01 and is reduced by 2/3 every 500 epochs).

Two different test sets (one for each case study) are generated by using the simulation strategy in Section IV. Test sets are simulated by setting $M = 2$ and h in accordance with the corresponding case study. For each test set we generated 10^3 surface spectral reflectance vectors $\boldsymbol{\rho}$ and the same number of adjacent spectral reflectance vectors $\boldsymbol{\rho}_a$. They are combined with the radiometric quantities generated by choosing at random the values of the aerosol parameter $IHAZE$ from the values reported in Table II. For the parameters V, ϑ and CWV all the values in Table III were considered. Notice that, test data differ from the training set for the surface reflectance vectors, the adjacent reflectance vectors and, also, for the values of the atmospheric parameters V, ϑ and CWV.

To test the estimation performance with respect to the noise affecting hyperspectral data, noisy at-sensor radiances are simulated. Noise realizations are generated according to the well-established signal dependent noise model proposed in [43] and [44]. They are drawn from a Gaussian distribution with zero mean and diagonal covariance matrix whose *k*-th diagonal element σ_k^2 linearly depends on the at-sensor radiance in the *k*-th sensor channel:

$$\sigma_k^2 = \sigma_{ph,k} L(\lambda_k) + \sigma_{th,k}^2 \tag{7}$$

where λ_k is the central wavelength of the *k*-th sensor channel, and $\sigma_{ph,k}$ and $\sigma_{th,k}^2$ account for the photon noise and the thermal noise, respectively. Specifically, we assume that the photon noise and the thermal noise terms have the same statistical

[1] It is worth noting that, the effect of the atmosphere on the radiative transfer in VNIR spectral range are actually negligible for altitude greater than 100 Km.

power per band, i.e. $\sigma_{ph,k}L(\lambda_k) = \sigma_{th,k}^2$. $\sigma_{ph,k}$ is modelled according to [43] as:

$$\sigma_{ph,k} = \frac{\beta}{\lambda_k \cdot m(\lambda_k)} \quad (8)$$

where $m(\lambda_k)$ is the sensor quantum efficiency and β is a multiplicative factor that allows the desired Signal to Noise Ratio (*SNR*) to be set. *SNR* is defined as the ratio between the total at sensor radiance power $\sum_{k=1}^{N_b} L^2(\lambda_k)$ and the total noise power $\sum_{k=1}^{N_b} \sigma_k^2$, and can be written as:

$$SNR = \frac{\sum_{k=1}^{N_b} L^2(\lambda_k)}{2\beta \sum_{k=1}^{N_b} \frac{L(\lambda_k)}{\lambda_k \cdot m(\lambda_k)}} \quad (9)$$

In eq. (9) N_b is the number of sensor channels. Eq. (9) makes explicit the dependence of the *SNR* on the multiplicative factor β. For $m(\lambda_k)$ we have not a specific model, it is approximated as a Gaussian function on the basis of the behavior of $\sigma_{ph,k}$ experienced in real data ([43]).

As stated in the first part of this Section, CWV-Net is compared with the LRSWE algorithm and the APDA algorithm. Both the algorithms require LUTs derived for specific values of the atmospheric visibility and the solar zenith angle. In the following comparative analysis, the LUTs adopted for the two algorithms are derived by setting $V = 35\ Km$ and $\vartheta = 0^{\circ}$.

LRSWE also needs the knowledge of the at-sensor radiance of the adjacent pixels $\boldsymbol{L}_a$. As to $\boldsymbol{L}_a$, in the derivation of the algorithm it was assumed that the *k*-th component of the vector is obtained by the RTM in eqs. (1) and (2) with $\rho(\lambda_k) = \rho_a(\lambda_k)$:

$$L_a(\lambda_k) = L_{GND}(\lambda_k) + L_p(\lambda_k)$$
$$L_{GND}(\lambda_k) = \frac{E_g(\lambda_k)}{\pi} \frac{\tau_1(\lambda_k) + \tau_2(\lambda_k)}{1 - S(\lambda_k)\rho_a(\lambda_k)} \rho_a(\lambda_k) \quad (7)$$

where, for simplicity, the dependence of the radiometric quantities on the atmospheric parameters has been omitted.

In general, $\boldsymbol{L}_a$ is obtained as a linear combination of the radiances of a neighborhood of the pixel under consideration. In this analysis, using the simulation strategy in Section IV (Figure 2), we generate also the vector $\boldsymbol{L}_a$ that is used as an input together with $\boldsymbol{L}$ for the LRSWE algorithm. Therefore, the algorithm is tested in the ideal condition in which there is no uncertainty on the value of $\boldsymbol{L}_a$.

Notice that both LRSWE and APDA work on a specific water absorption band. In the following analysis, we consider the water absorption band around 820 nm. Such choice is made to avoid the bias due to leaf water content generally experienced over vegetated pixels.

As to LRSWE the low rank subspace reflectance matrix in the selected absorption band is derived from the library **D**, by the Singular Value Decomposition (SVD) based procedure described in [17].

In applying both the algorithms, the data are binned with a factor of two and in the case of CWV-Net the bands with central wavelength greater than 925 nm are discarded.

Performance are evaluated in terms of $MAPE$ between the estimation provided by each algorithm and the value of CWV with which the data are simulated.

Table III. Variable atmospheric parameters adopted in simulating the test sets.

Atmospheric Parameters in the test sets	
$\vartheta(deg)$	0, 5:10:45
$V(Km)$	15:10:65, 100
$CWV\ (^{g}/_{cm^2})$	0.5:0.25:5

B. Aerial scenario: results and discussion.

Figure 3 , which refers to a flight height of 1 Km, shows the values of $MAPE$ obtained for all the CWV values in Table III by varying V (according to Table III). The figure was obtained in the absence of noise and with the same a solar zenith angle of 0 degrees adopted to derive the LUTs for both LRSWE and APDA. The total number of test data generated in this case study is $6.65 \cdot 10^5$.

Figure 3 shows that CWV-Net has good estimation performance with values of $MAPE$ in the order of 1.2% and that CWV-Net has approximately the same estimation performance regardless of the value of V. In particular, results in Figure 3 show that CWV-Net provides good estimation performance without any knowledge of the adjacent at sensor radiance and of the atmospheric visibility value.

As expected, this conclusion cannot be extended to the LRSWE algorithm. It outperforms CWV-Net providing the lowest value of $MAPE$ (0.44%) for $V = 35\ Km$, which is the visibility value adopted in the derivation of the LUT. However, the performance degrades when the atmospheric visibility deviates from the hypothesized value. LRSWE is outperformed by CWV-Net for all the considered V values with the exception of $V = 35\ Km$ and $V = 45\ Km$.

The APDA algorithm provides performance worse than that attained by CWV-Net. Figure 3 also shows that APDA has the best performance ($MAPE = 2.4\%$) for the visibility value adopted to derive the LUT ($V = 35\ Km$). The performance worsens when the atmospheric visibility of the test data deviates from that value.

Furthermore, Figure 3 confirms the conclusion drawn in [17] i.e.: LRWSE generally outperforms APDA.

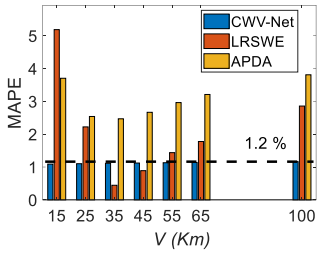

Figure 3. h=1 Km: Estimation performance in terms of $MAPE$ of CWV-Net, LRSWE and APDA for different values of V and obtained in absence of noise and with $\vartheta = 0^{\circ}$.

Figure 4 (a) and (b) show the results obtained in presence of noise with SNR equal to 50 dB and 35 dB, respectively.

Note that, even in the presence of noise, CWV-Net provides the same estimation performance for all the values of the parameter V. They also show that CWV-Net performance degrades with decreasing SNR. Specifically, for CWV-Net, values of $MAPE$ are below by 1.3% for $SNR = 50\,dB$ and 3.8% for $SNR = 35\,dB$. Comparing the results provided by CWV-Net with those of LRSWE we can see that the DNN based algorithm is more robust to noise. In fact, the increase in $MAPE$ values with decreasing SNR is more significant for LRSWE than for CWV-Net. In the ideal case of $V = 35\,Km$ and $\vartheta = 0^{\circ}$, LRSWE yields MAPE values equal to 0.44% in absence of noise, 0.9% with $SNR = 50\,dB$ and 4.4% with $SNR = 35\,dB$. Similar conclusions can be drawn by comparing CWV-Net with APDA. It is worth noting that, also in the presence of noise, APDA performance degrades when test data visibility deviates from the value adopted to derive the LUT.

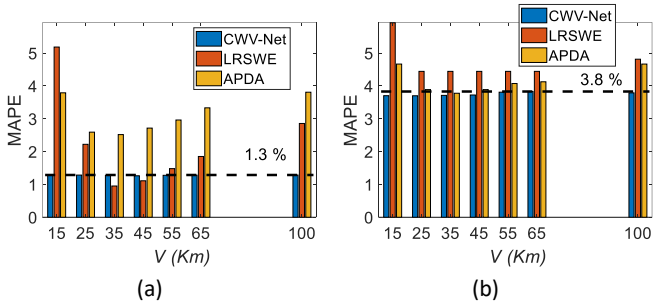

Figure 4. h=1 Km: Estimation performance in terms of $MAPE$ of CWV-Net, LRSWE and APDA for different values of V, with $\vartheta = 0^{\circ}$ and with $SNR = 50\,dB$ (a) and $SNR = 35\,dB$ (b).

In Figure 5 (a)-(c), we test the performance of the three algorithms for the values of the solar zenith angle in Table III, and assuming V = 35 Km,. The total number of test data generated is $6.65 \cdot 10^5$. Figure 5 (a) refers to the case of noise free data, while Figure 5 (b) and (c) show the results obtained with SNR equal to 50 dB and 35 dB, respectively.

Here again, in absence of noise, CWV-Net provides very low values of $MAPE$, in the order of 1.1%. Furthermore, Figure 5 (a) shows that the performance of CWV-Net is approximately the same for all the values of ϑ. This is confirmed also in the noisy cases where, of course, the performance degrades with decreasing SNR. With high SNR (50 dB), CWV-Net yields very low values of $MAPE$ (1.3%). The error index grows up to 3.7% when SNR decreases to 35 dB. As opposite to CWV-Net, the performance of both LRSWE and APDA strongly depends on the values of ϑ. Particularly, the estimation error increases as ϑ deviates from the value ($\vartheta = 0^{\circ}$) used to compute the LUTs adopted by the two algorithms. To give some numerical examples, in the case of LRWSE and in absence of noise, $MAPE$ goes from 0.44% in the ideal case ($V = 35\,Km$ and $\vartheta = 0^{\circ}$) to 36% when $\vartheta = 45^{\circ}$. In the case of APDA (in absence of noise) $MAPE$ has its minimum value (2.4%) in the ideal case and grows up to 31% when $\vartheta = 45^{\circ}$.

It is worth noting that, we obtained similar results by considering flight heights of 2 Km and 3 Km.

C. Satellite scenario: results and discussion.

Experiments similar to those presented in Sub-section V.B are carried out in the case of a satellite scenario, where the contribution of CWV on the at-sensor radiance is more significant than in the aerial scenario as the electromagnetic radiation follows a longer path upwards.

Figure 6 a)-c) show $MAPE$ values for the three algorithms obtained by letting ϑ to 0 and by varying V and the contribution of noise. In the absence of noise (Figure 6 a)) CWV-Net has approximately the same performance for all values of V.

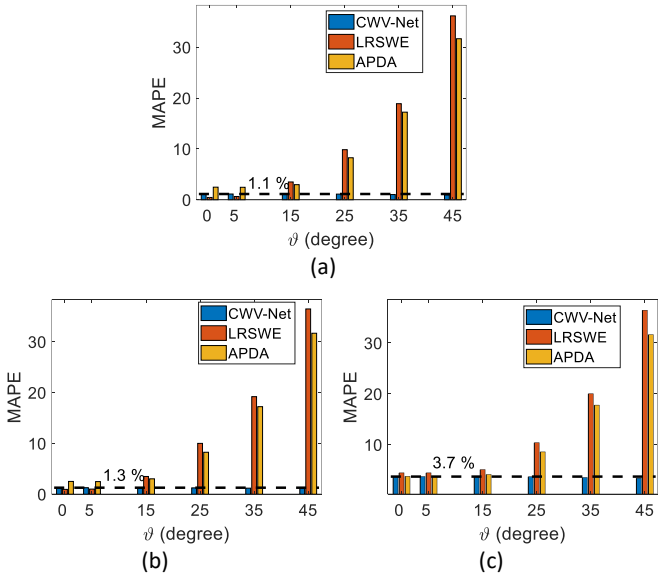

Figure 5. h=1 Km: Estimation performance in terms of $MAPE$ of CWV-Net, LRSWE and APDA for different values of ϑ, obtained with V=35 Km in absence of noise (a), with $SNR = 50\,dB$ (b) and with $SNR = 35\,dB$ (c).

Specifically, it provides values of $MAPE$ lower than 1.2%. The performance of LRSWE varies with V. The best result ($MAPE = 0.37\%$) is obtained in the ideal case of $V = 35\,Km$. However, in this case, LRSWE outperforms CWV-Net for all values of V except for $V = 15\,Km$ and $V = 100\,Km$. APDA

attains the best performance ($MAPE = 1.7\%$)) for the value of V equal to that adopted to derive the LUT ($V = 35\ Km$). Its performance degrades slightly for $V > 35\ Km$. the worst performance is obtained for $V = 15\ Km$. Results confirm that the LRSWE performs better than APDA ([17]).

In presence of moderate noise contribution ($SNR = 50\ dB$, Figure 6 b)) the performance of CWV-Net remains constant ($MAPE$ in the order of 1.4%) with respect to V and are similar to that provided by LRSWE. When SNR drops to $35\ dB$ (Figure 6 c)), CWV-Net outperforms LRSWE by providing values of $MAPE$ lower than 3%. APDA seems to be more robust to noise with respect to LRSWE. However, APDA provides lower accuracy than CWV-Net in all the considered cases.

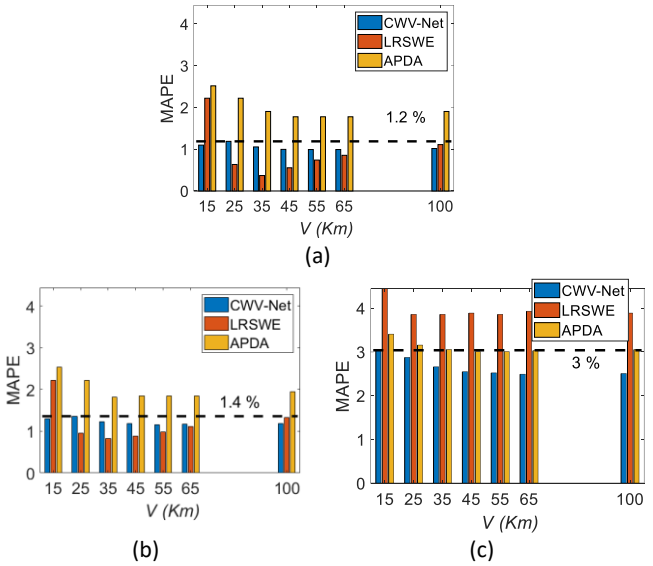

Figure 6. *Satellite scenario*: CWV-Net, LRSWE and APDA estimation performance in terms of $MAPE$ for different values of V, obtained with $\vartheta = 0^{\circ}$: (a) absence of noise, (b) $SNR = 50\ dB$, (c) $SNR = 35\ dB$ (c).

Setting $V = 35\ Km$ and varying ϑ, the three algorithms yield the performance shown in Figure 7 a)-c). Results show the robustness of CWV-Net with respect to ϑ in all the cases of noise absent, $SNR = 50\ dB$ and $SNR = 35\ dB$. Specifically, CWV-Net has very low values of $MAPE$ ($\leq 1.2\%$) with moderate (Figure 7 b)) or absent noise (Figure 7 a)). $MAPE$ increases (while remaining below 3%) when SNR drops to $35\ dB$ (Figure 7 c)). On the contrary, the performance of LRSWE degrades when the difference between the values of ϑ adopted in the LUT and that of the observed data increaes. This behavior is confirmed for all the cases considered in our experiment and is observed also for the APDA algorithm.

We would like to remark again that in all the experiments discussed in this Section, LRSWE has been tested with no uncertainty on the value of $\boldsymbol{L}_a$. This is an ideal condition that generally does not occur in real applications where $\boldsymbol{L}_a$ must be estimated from the analyzed image by assuming an atmospheric PSF model.

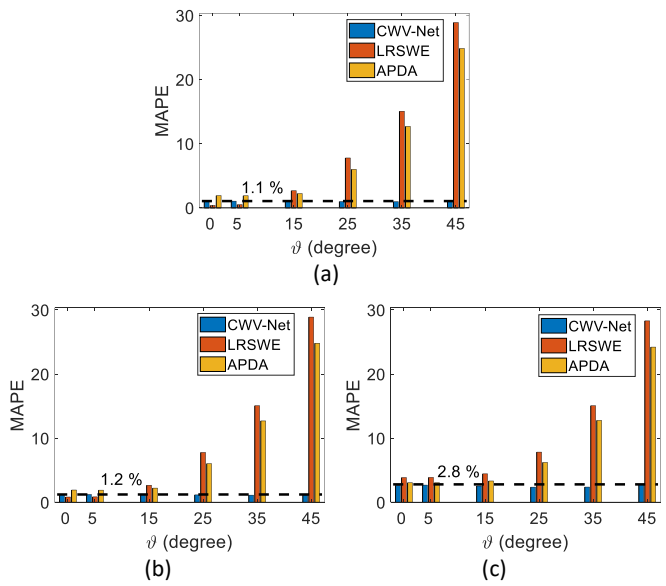

Figure 7. *Satellite scenario*: CWV-Net, LRSWE and APDA estimation performance in terms of $MAPE$ for different values of ϑ, obtained with V=35 Km: a) absence of noise. (b) $SNR = 50\ dB$, (c) $SNR = 35\ dB$.

VI. Example over real data

In this Section, we present the results obtained by applying CWV-Net to a real hyperspectral image. It important to note that, evaluating the performance of any CWV retrieval algorithm on real data is impractical. Indeed, performance analysis would require a great amount of hyperspectral data including precise measurements of the parameter CWV that varies spatially over the scene. Unfortunately, there are no data set available that meet these requirements. Therefore, simulation remains the only way to perform accurate performance analysis and comparison and to draw reliable conclusions.

The lack of information about the CWV values at the time of the acquisition and the uncertainty on the radiometric calibration of the data, prevent the assessment and the comparison of the performance provided by CWV-Net, the LRSWE algorithm and the APDA algorithm over the selected data set. The example reported in the following provides a proof of concept aimed at showing that CWV-Net produces plausible results over real data.

The hyperspectral image adopted in our example is part of the data set acquired during the "Viareggio 2013 trial" that was held in Viareggio (Italy), on May 8 and 9, 2013 ([45]). All the data were collected by the SIM.GA sensor introduced in Section III. For this experiment, we focus on the image named D2F22H2 that was acquired on May 9, 2013 under clear sky conditions over a scene including a parking lot (where a number of man-made objects were deployed), several sport facilities buildings, and a football field. The flight height was of about 1.2 Km that corresponds to a nominal ground spatial resolution of about 0.6 m.

The image is equipped with ground truth data including the map of the deployed man-made objects (targets) and their spectral reflectances measured by an ASD FieldSpec hand-held spectroradiometer. In Figure 8 we show the Red Green Blue (RGB) representation of the image and, superimposed, the locations of the man-made objects. Each object is identified by a label.

For this example, CWV-Net was trained according to the procedure described in Section IV. Specifically, the training set was generated by setting $h = 1.2\,Km$ and the MODTRAN parameter M to 2 corresponding to Mid-latitude summer. This choice is motivated by the geographical coordinates of the scene and by the fact that acquisition was made in the late spring season.

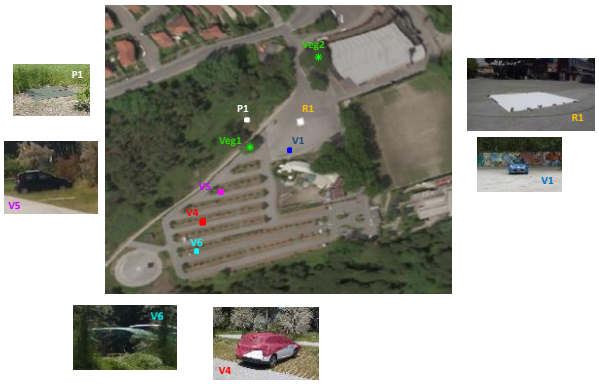

Figure 8. RGB representations of the hyperspectral image adopted in the example.

The CWV values expressed in $g \cdot cm^{-2}$ provided by the network for each pixel of the image are reported in the map of Figure 9.

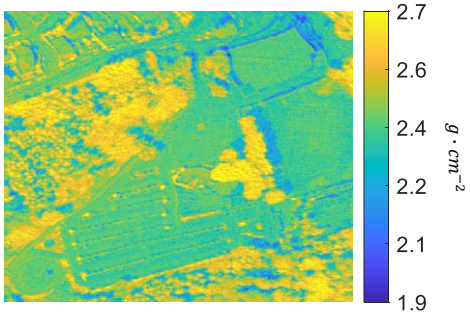

Figure 9. CWV estimates obtained by applying CWV-Net to each pixel of the image.

Comparing the CWV map in Figure 9 with the RGB image in Figure 8 we can note that the lowest values of CWV are obtained in the shadowed areas. The proposed algorithm does not provide reliable results in those areas because the adopted RTM does not account for the shadow effects. In the remaining pixels of the image CWV-Net provides values in the range $[2.3, 2.7]\ g \cdot cm^{-2}$.Specifically, the mean value of the estimated CWV is $2.46\ g \cdot cm^{-2}$ and its standard deviation is $9 \cdot 10^{-2}\ g \cdot cm^{-2}$. The obtained values are compliant with those that characterize, at least on a large scale, the region of the world that includes the monitored site.

As already stated, in the absence of CWV real value measurements, it is not possible to carry out a quantitative assessment of the algorithm's performance. However, one can obtain a sort of indirect validation by analyzing the reflectance spectrum obtained inverting the RTM for some of the image pixels and making use of the values of CWV estimated by CWV-Net.

In order to invert the RTM (Atmospheric Compensation), we need the values of the other relevant MODTRAN parameters and specifically: ϑ, V and the aerosol model defined by the parameter $IHAZE$. The value of ϑ is obtained considering the geographical coordinates of the monitored scene and the acquisition date and time. While the values of $IHAZE$ and V are estimated by using the Boundary Shaded Pixels based algorithm proposed in [9]. This latter provides $V = 33\,Km$ and $IHAZE = 4$ corresponding to the "Maritime" aerosol type.

Atmospheric compensation is applied to several pixels of the image. In Figure 10 we show the results (red plot) obtained for the target labelled as R1 (Figure 8). It is a white calibration tarp that was adopted for its isotropic reflective behavior that makes it a good approximation of a Lambertian surface. Figure 10 also shows the spectral reflectance of R1 measured by the FieldSpec instrument and included in the ground truth metadata. The transparent blue patches highlight the water absorption bands. The high similarity between the atmospheric compensated spectrum and the measured one in those bands, shows that CWV value provided by CWV-Net allows the water absorption to be correctly compensated. Notice that for completeness, in Figure 10 we report the value of CWV ($2.497\ g \cdot cm^{-2}$) provided by CWV-Net in the pixel occupied by R1.

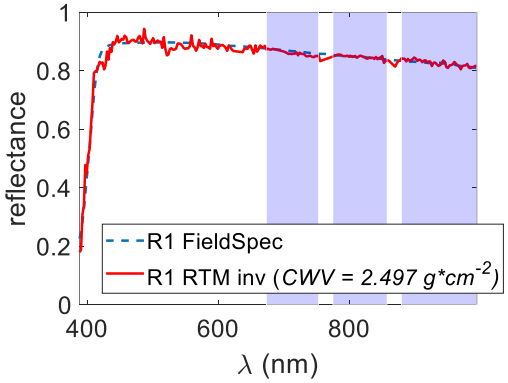

Figure 10. Target R1: comparison between the reflectance spectrum measured by the FieldSpec instrument and that obtained from the image by inverting the RTM and using the CWV estimate provided by CWV-Net.

To give an example, we applied also the APDA algorithm to the real image presented in this section by considering the water absorption band around 820 nm. In Figure 11 we plot the results

of the atmospheric compensation on the target R1 obtained by using the CWV estimates provided by the APDA algorithm in three cases. In the first case (red line), APDA is applied by using the LUT derived with the correct visibility value ($V = 33\ Km$). In this case, we obtain a result very similar to that provided by CWV-Net that does not use any *a-priori* knowledge of either the solar zenith angle or the atmospheric visibility. Specifically, the estimated value of CWV (2.5 $g \cdot cm^{-2}$) is very close to that provided by CWV-Net (2.497 $g \cdot cm^{-2}$).

In the other two cases, we used the LUT derived with incorrect values of V. Specifically, the green plot is obtained for $V = 60\ Km$ and the black line is obtained for $V = 15\ Km$. The CWV estimates provided by the APDA algorithm in the two cases are 2.6 $g \cdot cm^{-2}$ and 2.4 $g \cdot cm^{-2}$, respectively. Notice that, in these two cases the retrieved reflectance spectra nearby 950 nm, differ from the spectral reflectance measured by the FieldSpec. This can be considered as an indirect proof of the errors induced on the APDA estimates by the incorrect visibility value adopted in deriving the LUT.

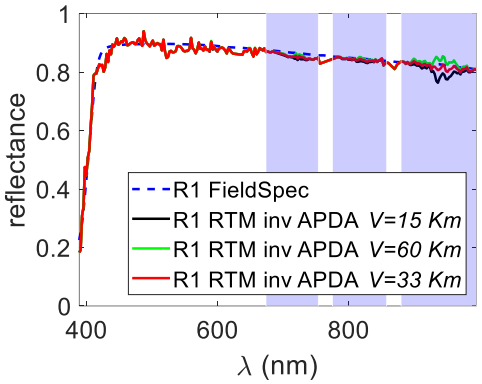

Figure 11. Target R1: comparison between the reflectance spectrum measured by the FieldSpec instrument and that obtained from the image by inverting the RTM and using the CWV estimates provided by APDA in the 820 nm absorption band. CWV estimates for RTM inversion are obtained by using the LUT derived with the correct visibility value (red line) and the LUTs derived with incorrect visibility values (green and black lines).

As another example of the results provided by the proposed CWV-Net, in Figure 12, we show the reflectance spectra obtained by inverting the RTM for two pixels of vegetation, those labelled as Veg1 and Veg2 in Figure 8. For those pixels, the FieldSpec measurements are not available. However, it is interesting to note how the water absorption features (blue patches) are correctly compensated. It is worth noting, that both the spectra have the classical behavior of the canopies where the absorption feature in the spectral region above 925 nm is due to the leaf water content.

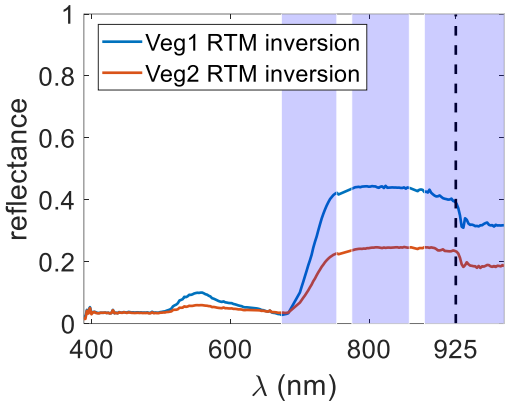

Figure 12. Reflectance spectra of the pixels labelled as Veg1 and Veg2 obtained by inverting the RTM.

For completeness, in Figure 13 a)-e) we compare the reflectance spectra of the other targets included in the ground truth with those obtained from the corresponding image pixels by inverting the RTM and using the CWV estimates provided by the proposed algorithm. Notice that, neither the adopted RTM nor the ASD FieldSpec account for the bidirectional reflectance distribution function (BRDF, [46]), whose effect is generally roughly approximated as a scaling factor. For this reason, in each figure we also plot the version of the measured FieldSpec spectrum scaled so as to have the same energy of the image retrieved spectrum. In all the figures, we can see that the water absorption is well compensated.

VII. Conclusions

In this paper, CWV-Net, a 1D-CNN based DNN, is proposed for the retrieval of the total column water vapor content of the atmosphere from VNIR hyperspectral images. CWV-Net works on each image pixel in order to account for the spatial variability of the parameter CWV within the observed scene. The network is specifically designed and trained to works without the knowledge of other significant atmospheric model parameters such as V, ϑ and the atmospheric PSF.

The network training involves synthetic data that are generated according to a well-established RTM, by using the Modtran radiative transfer code and available spectral reflectance libraries.

Results on simulated data have shown the potential and flexibility of the DNN-based approach in estimating CWV independently of the values of V and ϑ and regardless of the adjacency effects. Specifically, results obtained in both aerial and satellite scenarios, showed that in the presence of moderate noise ($SNR = 50dB$), CWV-Net has estimation error in the order of 1%. Such an error increases when SNR decreases. However, for $SNR = 35\ dB$ the error remains less than 4%.

The application of CWV-Net to a real hyperspectral image has shown that the DNN-based approach provides reasonable results even outside the controlled environment of the simulated data.

It is worth noting that, the DNN-based approach offers an additional advantage concerning the computational load.

Although training is generally computationally expensive, applying CWV-Net to a given image requires a low computational load that makes the proposed approach suitable for real time applications. Just to give an example, by using a MATLAB implementation on a personal computer equipped with Intel Core i7-4820K CPU at 3.7 GHz and with a 16 GB of RAM, we experienced a computing time of about 7 μs per pixel (228 elements vector). To process the real image of Section VI having 450x375 pixels, our MATLAB implementation of CWV-Net took a total time of 1.2 s. Processing times can be significantly reduced using dedicated hardware or modern Graphical Processing Units.

We would like to conclude by noting that, CNN architectures generally provide a certain degree of invariance with respect to input nodes shift, which could be useful for obtaining the robustness of the algorithm with respect to spectral mis-calibration. This issue requires further investigation and is one of the objectives of our ongoing activities. Future activities will also concern the analysis of the impact of the radiometric mis-calibration on the performance of CWV-Net and the study of possible methods to reduce this impact.

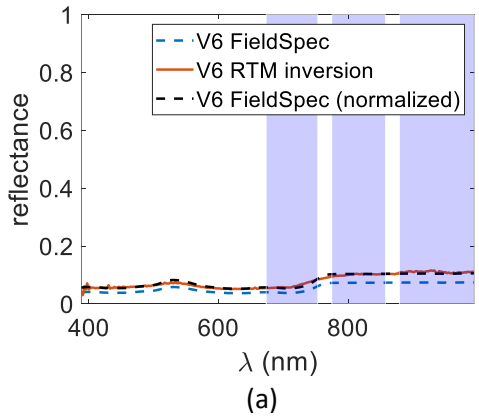

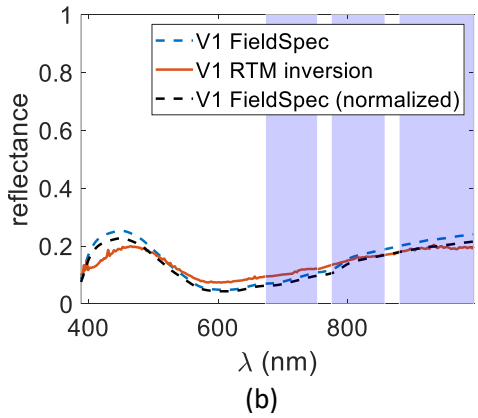

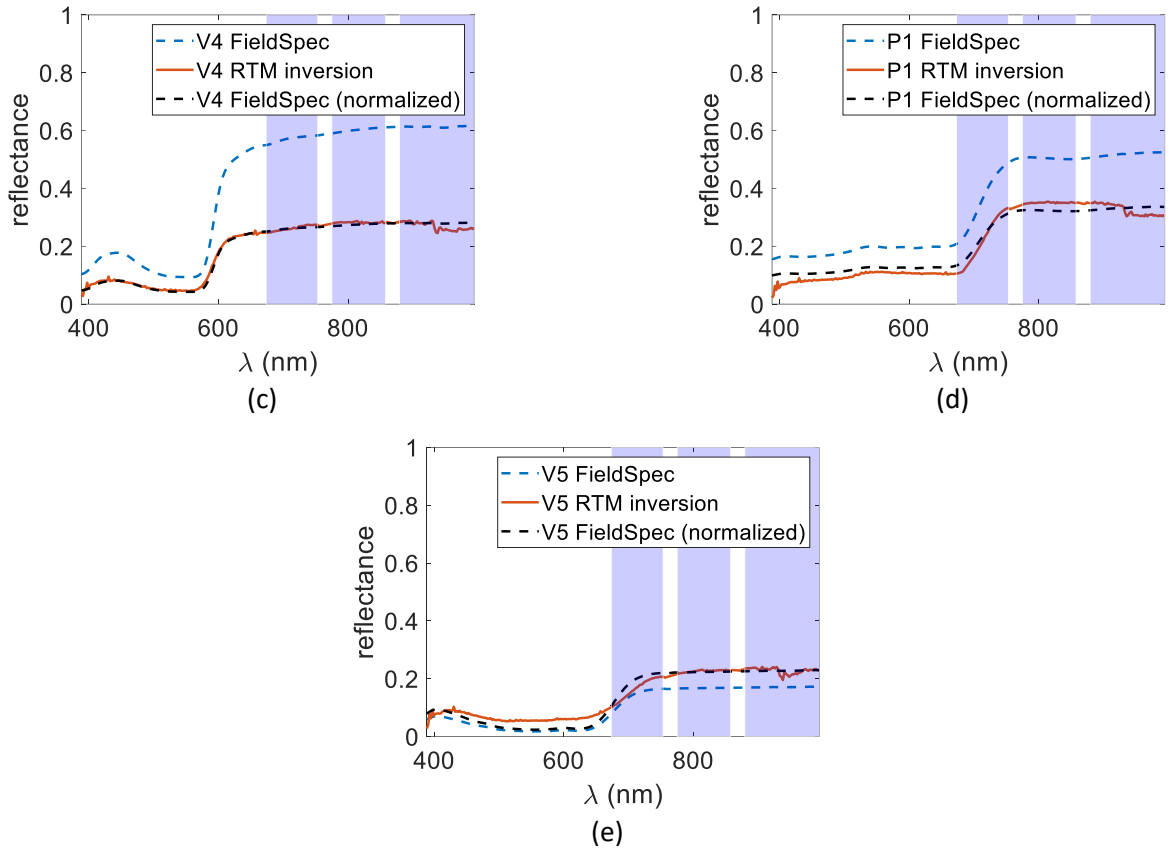

Figure 13. Comparison between the reflectance spectrum measured by the FieldSpec instrument, its scaled version and that obtained from the image by inverting the RTM for the ground truth targets: V6 (a), V1 (b), V4 (c), P1 (d) and V5 (e).

REFERENCES

[1]. http://www.headwallphotonics.com.

[2]. http://www.hyspex.com.

[3]. http://www.itres.com.

[4]. B.-C. Gao, M. J. Montes, C. O. Davis, A. F. H. Goetz, "Atmospheric correction algorithms for hyperspectral remote sensing data of land and ocean", Remote Sensing of Environment, Vol. 113, pp. S17-S24, Sep. 2009.

[5]. M. K. Griffin and H. K. Burke, "Compensation of Hyperspectral Data for Atmospheric Effects," Lincolm Laboratory Journal, Vol. 14, No. 1, pp. 29-54, 2003.

[6]. B. -C. Gao, K. B. Heidebrecht, and A. F. H. Goetz, "Derivation of scaled surface reflectances from AVIRIS data," Remote Sensing of Environment, Vol. 44, pp. 165−178, 1993.

[7]. F. A. Kruse, "Comparison of ATREM, ACORN, and FLAASH atmospheric corrections using low-altitude AVIRIS data of Boulder, CO," Summaries of 13th JPL Airborne Geoscience Workshop, Jet Propulsion Lab, Pasadena, CA. (2004).

[8]. R. Richter and D. Schlaepfer, "Geo-atmospheric processing of airborne imaging spectrometry data. Part 2: atmospheric/topographic correction," International journal of Remote Sensing, Vol. 23, No. 1, pp. 2631-2649, 2002.

[9]. N. Acito, M. Diani, "Unsupervised Atmospheric Compensation of airborne hyperspectral images in the VNIR spectral range," IEEE Trans. on Geoscience and Remote Sensing, Vol. 56, No. 7, , pp. 3924-3940, 2018.

[10]. D. Manolakis, R. Lockwood, T. Codey, "Hyperspectral imaging remote sensing", Cambridge University Press, 2016.

[11]. R. Richter, D. Schlaepfer and A. Muller, "An automatic atmospheric correction algorithm for visible/NIR imagery," International Journal of Remote Sensing, Vol. 27, No. 10, pp. 2077-2085, May 2006.

[12]. S.M. Adler-Golden, A. Berk, L.S. Bernstein, S. Richtsmeier, P.K. Acharya, M.W. Matthew, G.P. Anderson, C. Allred, L. Jeong, and J. Chetwynd, "FLAASH, A MODTRAN4 Atmospheric Correction Package for Hyperspectral Data Retrievals and Simulations," Proc. 7th Ann. JPL Airborne Earth Science Workshop, JPL Publication 97-21, Pasadena, Calif., pp. 9–14, 1998.

[13]. D Schlaepfer, C. C. Borel, J. Keller and K. I. Itten, "Atmospheric Precorrected Differential Absorption Technique to Retrieve Columnar Water Vapor," Remote Sensing of Environment, Vol. 65, No. 3, pp: 353-366, Sept. 1998.

[14]. R. Richter and D. Schlaepfer, "Geo-atmospheric processing of airborne imaging spectrometry data. Part 2: atmospheric/topographic correction," International journal of Remote Sensing, Vol. 23, No. 1, pp. 2631-2649, 2002.

[15]. J. R. Schott, Remote Sensing: The Image Chain Approach, 2nd ed., New York: Oxford University Press, 2007.

[16]. C. Miesh, L. Poutier, V. Achard, X. Briottet, X. Lenot and Y. Boucher, "Direct and Inverse Radiative Transfer Solutions for Visible and Near-Infrared Hyperspectral Imagery," IEEE Trans. on Geoscience and Remote Sensing, Vol. 43, No. 7, pp. 1552-1562, July 2005.

[17]. N. Acito, M. Diani, "Atmospheric Column Water Vapor Retrieval from Hyperspectral VNIR Data Based on Low-Rank Subspace Projection," IEEE Trans. on Geoscience and Remote Sensing, Vol. 56, No. 7, pp. 3924-3940, July 2018.

[18]. A. Berk, L. S. Bernstein and D. C. Robertson, "MODTRAN: A Moderate Resolution Model for LOWTRAN 7," Spectral Sciences, Burlington, MA, GLTR890122, 1989.

[19]. A. A. Semenov, A. V. Moshkov, V. N. Pozhidayev, A. Barducci, P. Marcoionni and I. Pippi, "Estimation of Normalized Atmospheric Point Spread Function and Restoration of Remotely Sensed Images," IEEE Trans. on Geoscience and Remote Sensing, Vol. 49, No. 7, pp. 2623-2634, July 2011.

[20]. T. Perkins, S. M. Adler-Golden, M.W. Matthew, A. Berk, L. S. Bernstein, J. Lee and M. J. Fox, "Speed and Accuracy Improvements in FLAASH Atmospheric Correction of Hyperspectral Imagery," SPIE Optical Engineering, Vol. 51, No. 11, pp. 111707-1,111707-7, 2012.

[21]. A. Signoroni, M. Savardi, A. Baronio, S. Benini, "Deep Learning Meets Hyperspectral Image Analysis: A Multidisciplinary Review," MDPI Journal of Imaging, Vol. 5, No. 5, pp. 1-32, May 2019.

[22]. P Ghamisi, N. Yokoya, J. Li, W. Liao, S. Liu, J. Plaza, B. Rasti, A. Plaza, "Advances in Hyperspectral Image and Signal Processing," IEEE Geoscience and Remote Sensing Magazine, Vol. 5, No. 4, pp. 37-78, Dec. 2017.

[23]. W. Hu, Y. Huang, L. Wei, F. Zhang, H. Li "Deep Convolutional Neural Networks for Hyperspectral Image Classification," Hindawi Journal of Sensors, Vol. 2015, 258619, pp. 1-12, 2015.

[24]. L. Mou, P. Ghamisi, X. X. Zhu, "Deep Recurrent Neural Networks for Hyperspectral Image Classification," IEEE Trans. Geosci. Remote Sens., Vol. 55, No. 7, pp 3639–3655, April 2017.

[25]. W. Zhao, Z. Guo, J. Yue, X. Zhang, L. Luo, "On combining multiscale deep learning features for the classification of hyperspectral remote sensing imagery," Int. J. Remote Sens., Vol. 36, No. 13, pp. 3368–3379, 2015.

[26]. Y. Li, W. Xie, H. Li, "Hyperspectral image reconstruction by deep convolutional neural network for classification," Pattern Recognit., Vol. 63, pp. 371–383, March 2017.

[27]. M. Zhang, W. Li, Q. Du, "Diverse Region-Based CNN for Hyperspectral Image Classification," IEEE Trans. Image Process., Vol. 27, No. 6, pp. 2623–2634, Feb. 2018.

[28]. Y. Chen, H. Jiang, C. Li, X. Jia, P. Ghamisi. "Deep Feature Extraction and Classification of Hyperspectral Images Based on Convolutional Neural Networks," IEEE Trans. on Geoscience and Remote Sensing, Vol. 54, No. 10, , pp. 6232-6251, July 2016.

[29]. J. Liang, J. Zhou, Y. Qian, L. Wen, X. Bai, Y. Gao, "On the Sampling Strategy for Evaluation of Spectral–spatial Methods in Hyperspectral Image Classification," IEEE Trans. Geosci. Remote Sens., Vol. 55, No. 2, pp. 862–880, Nov. 2016.

[30]. W. Xie, Y. Li, X. Jia, "Deep convolutional networks with residual learning for accurate spectral–spatial denoising," Neurocomputing, Vol. 312, pp. 372–381, Oct. 2018.

[31]. W. Xie, Y. Li, J. Hu, D. Y. Chen, "Trainable spectral difference learning with spatial starting for hyperspectral image denoising," Neural Networks, Vol. 108, pp. 272–286, Dec. 2018.

[32]. P.N. Reinersman and K. L. Carder, "Monte Carlo simulation of the atmospheric point-spread function with application to correction for adjacency effect", Applied Optics, Vol. 34, No. 21, pp. 4453-4471, July 1995.

[33]. Y. LeCun;, B. Boser, J.S. Denker, R.E. Howard, W. Habbard, L.D. Jackel, "Handwritten Digit Recognition with a BackPropagation Network," Advances in Neural Information Processing Systems (NIPS 1989), Denver, CO (Vol. 2). Morgan Kaufmann, pp. 396–404, 1990.

[34]. K.F. Palmer, D. Williams, "Optical properties of water in the near infrared," Journal of the Optical Society of America, Vol. 64, pp. 1107– 1110, 1974.

[35]. D. A. Sims, J. A. Gamon, "Estimation of vegetation water content and photosynthetic tissue area from spectral reflectance: a comparison of indices based on liquid water and chlorophyll absorption features," Remote Sensing of Environment, Vol. 84, pp. 526-537. 2003.

[36]. A.M. Baldridge, S.J. Hook, C.I. Grove and G. Rivera, "The ASTER Spectral Library Version 2.0," Remote Sensing of Environment, Vol 113, pp. 711-715, 2009.

[37]. R.N. Clark, G.A. Swayze , R.A. Wise, K.E. Live, T.M. Hoefen, R.F. Kokaly, and S.J. Sutley, USGS Digital Spectral Library splib06a: U.S. Geological Survey Data Series 231, 2007.

[38]. Available on line at http://opticleaf.ipgp.fr/index.php?page.

[39]. D. C. Heinz, C. Chang, "Fully constrained least squares linear spectral mixture analysis method for material quantification in hyperspectral imagery," IEEE transactions on geoscience and remote sensing, Vol. 39, No. 3, pp. 529-545, Mar. 2001.

[40]. A. Berk , G.P. Anderson , P.K. Acharya , E.P. Shettle, "MODTRAN®5.2.0.0 USER'S MANUAL," instrumentation.tamu.edu/~ting/other/MODTRAN(R)5.2.0.0.doc.

[41]. K. P. Murphy, Machine Learning: A Probabilistic Perspective. The MIT Press, Cambridge, Massachusetts, 2012.

[42]. D.P. Kingma, J. L.Ba, "Adam: A method for stochastic optimization," 3rd International Conference on Learning Representations, ICLR, pp. 1-15, 2015.

[43]. T. Skauli, "Sensor noise informed representation of hyperspectral data, with benefits for image storage and processing," Optics Express, Vol. 19, No. 14, pp. 13031-13046, June 2011.

[44]. N. Acito, M. Diani, G. Corsini, "Signal-Dependent Noise Modeling and Model Parameter Estimation in Hyperspectral Images," IEEE Trans. on Geos. and Rem. Sensing, Vol. 49, No. 8, pp. 2957-2971, August 2011.

[45]. N. Acito, S. Matteoli, A. Rossi, M. Diani, G. Corsini, "Hyperspectral Airborne "Viareggio 2013 Trial" Data Collection for Detection Algorithm Assessment," IEEE Journal of Selected Topics in Applied Earth Observations and Remote Sensing, Vol. 9, No. 6, pp. 2365-2376, 2016.

[46]. E. J. Ientilucci, M. Gartley, "Impact of BRDF on physics-based modeling as applied to target detection in hyperspectral imagery," Proc. SPIE 7334, Algorithms and Technologies for Multispectral, Hyperspectral, and Ultraspectral Imagery XV, 73340T (27 April 2009).